Opto-Electronic Advances

Original Article

2021, Vol. 4, No. 10

DOI: 10.29026/oea.2021.200029

Optical properties and applications of SnS_2 SAs with different thickness

Mengli Liu[1], Hongbo Wu[2], Ximei Liu[1], Yaorong Wang[1], Ming Lei[1], Wenjun Liu[1,3]*, Wei Guo[2]* and Zhiyi Wei[3]*

Q-switched lasers have occupied important roles in industrial applications such as laser marking, engraving, welding, and cutting due to their advantages in high pulse energy. Here, SnS_2-based Q-switched lasers are implemented. Considering that SnS_2 inherits the thickness sensitive optical characteristics of TMD, three kinds of SnS_2 with different thickness are characterized in terms of nonlinearity and used to realize the Q-switched pulses under consistent implementation conditions for comparison tests. According to the results, the influence of thickness variation on the nonlinear performance of saturable absorber, such as modulation depth and absorption intensity, and the influence on the corresponding laser are analyzed. In addition, compared with other traditional saturable absorbers, the advantage of SnS_2 in realizing ultrashort pulses is also noticed. Our work explores the thickness-dependent nonlinear optical properties of SnS_2, and the rules found is of great reference value for the establishment of target lasers.

Keywords: nonlinear optical materials; fiber laser; Q-switching

Liu ML, Wu HB, Liu XM, Wang YR, Lei M et al. Optical properties and applications of SnS_2 SAs with different thickness. *Opto-Electron Adv* **4**, 200029 (2021).

Introduction

Q-switching and mode-locking technologies, as two main methods to realize pulsed output in laser cavities, have been widely concerned in recent years[1–3]. However, the preferred application fields of the two are a little bit different. Specifically, mode-locked fiber lasers (MLFL) could achieve femtosecond pulses, the peak power and repetition rate of which are relatively high, therefore they are often used in devices with large resolution and fineness, but their pulse energy is low, generally in the order of pJ[4–5]. Q-switched fiber lasers (QSFL) can achieve pulse energy in the order of nJ or even higher due to the kHz repetition rate and high output power[6]. Therefore, they are commonly used in laser marking, carving, welding and cutting, etc. Although both active and passive methods can be used as effective ways to achieve Q-switching, passive one is usually preferred because of its obvious advantages, such as robustness, compact structure, as well as the unnecessity of complex electronic devices, which makes the passive method show an economic and effective application prospect[7].

With the development and expansion of some materials in recent years, the use of saturable absorbers (SAs) to achieve QSFLs has become the general trend[8–9]. As a more preferred option for SAs, semiconductor saturable absorption mirrors (SESAMs) were initially the focus of research[10]. However, the shortcomings of SESAMs, such as the preparation complexity, narrow bandwidth, and

[1]State Key Laboratory of Information Photonics and Optical Communications, School of Science, P. O. Box 91, Beijing University of Posts and Telecommunications, Beijing 100876, China; [2]School of Physics, Beijing Institute of Technology, 5 South Zhongguancun Street, Beijing 100081, China; [3]Beijing National Laboratory for Condensed Matter Physics, Institute of Physics, Chinese Academy of Sciences, Beijing 100190, China.
*Correspondence: WJ Liu, E-mail: jungliu@bupt.edu.cn; W Guo, E-mail: weiguo7@bit.edu.cn; ZY Wei, E-mail: zywei@iphy.ac.cn
Received: 10 July 2020; Accepted: 29 September 2020; Published online: 25 October 2021

high cost force scientists to find other feasible alternatives, especially those that can further improve the overall efficiency and compactness while ensuring high optical nonlinearity of the device[11]. The discovery of graphene solved the urgent development demand of QSFLs, and further pushed the development of SA to a new climax[12]. Soon, a lot of latterly developed materials with similar properties are explored to be the possible choices of SAs, including graphene analogues such as transition metal dichalcogenides (TMDs), topological insulators (TIs), and exotic materials such as black phosphorus (BP), nanowires[13–17].

Most recently, the investigation of TMDs has become a research hotspot. After going through sufficient research on WS_2 and MoS_2[18–19], another TMD, tin disulfide (SnS_2), has begun to attract widespread attention[20]. On the one hand, SnS_2 shows good oxidation resistance, which is of great benefit in improving system stability and robustness[21]. On the other hand, SnS_2 has the advantages of low cost, environmental friendliness, and sufficient global reserves, which allows it to meet the application needs of industrial and scientific full-scale production[22]. SnS_2 has a wider band gap than most TMDs, which is more suitable in some electronic applications[23–24]. In addition, its application potential in the fields of energy storage, photocatalysts, and field emission devices cannot be underestimated[25]. Meanwhile, the exceptional saturation absorption capabilities of SnS_2 prompts it to be widely studied in fiber laser applications[26–29]. However, most of the current implementations are mode-locked pulses, and there is only one report on QSFL[30]. Obviously, there is a lack of more systematic research on the impact of SnS_2 SA on QSFLs.

In this paper, the thickness-sensitive nonlinear characteristics of SnS_2 and the performance of lasers based on the corresponding SnS_2 SA are investigated. Three SnS_2 SAs with different thicknesses are prepared by the chemical vapor transport (CVT) technique combined with physical transfer method. The thickness information of those are characterized by atomic force microscope (AFM). The traditional balanced twin detector technique is applied to measure the nonlinear optical properties of SnS_2 SAs. Under the consistent experimental conditions, those SAs are applied to the laser respectively, and the experimental results are compared and analyzed. Our results explore the internal influence of material thickness on optical nonlinearity, which provide guidance for choosing a suitable SnS_2 SA to implement the QSFL with specific requirements, and also provide a good reference for the future research of nonlinear optical characteristics of similar TMD.

The preparation and characterization of SAs

Here, the CVT technique is chosen as the preparation method to ensure the high quality of SnS_2 materials. Before the experiment, the required precursors, such as Sn and S powders with a purity of up to 99% purchased from Sigma-Aldrich, and the transport agent iodine, were placed in the reaction chamber. Due to the temperature gradient settings of different parts of the reaction chamber, the gaseous raw materials with high-temperature were deposited on the substrate surface in the low-temperature region with carrier gas, forming SnS_2 crystal with high purity. The prepared SnS_2 crystal was then peeled into thin flakes with different thickness by mechanical exfoliation (ME). The combination of CVT and ME plays a dual role in ensuring the quality of SnS_2. The obtained flakes with a certain thickness were further transferred to the fiber ceramic head by the PMMA (poly methyl methacrylate) transfer method. The steps of transfer are as follows: firstly, PMMA solution was spin coated on the flakes at a speed of 3000 rpm. Then, the spin-coated material was heated at 150 °C for 30 minutes. Finally, the substrate with the attached SnS_2-PMMA was submerged in a NaOH solution at the temperature of 80 °C, and the SnS_2-PMMA were easily removed. Later, acetone was used as solvent to remove useless PMMA and avoid unnecessary heat accumulation. During the transfer process, the microscope ensures that each SnS_2 flake was placed in the center of the ceramic head, completely covering the light passing holes on it.

The X-ray diffraction patterns, high-resolution TEM image and X-ray photoelectron spectroscopy of SnS_2 samples are given in our previous research[29], which further confirmed that the synthesized SnS_2 owns high quality crystal structure. A lot of materials were tried in the experiment. After removing the data that could not be ruled out whether it was an experimental error, three sets of data with obvious characteristics that may indicate regularity were screened for display. The selected materials with obvious data changes have a large thickness span, which may be caused by the inhomogeneity of the related properties of SnS_2[31]. The specific morphology and thickness were characterized by AFM. The thickness of thicker SnS_2 was measured as 107 nm as revealed in Fig.

1(a) and 1(d). Similarly, the thicknesses of medium and thinner flakes are 7.7 nm (Fig. 1(b) and 1(e)) and 4 nm (Fig. 1(c) and 1(f)).

SAs generally exhibit traditional intensity-related light transmittance. In detail, most of low-intensity lights are absorbed, while high-intensity lights pass through with low loss. This light intensity-dependent absorption characteristic can be theoretically described by the following formula,

$$\alpha = \alpha_{ns} + \frac{\alpha_s}{1 + I/I_{sat}} . \quad (1)$$

where α exhibits the total absorption of material, α_{ns} is non-saturable loss, α_s is modulation depth, I is light intensity, I_{sat} is saturation intensity. The insertion loss (IL) of SA is able to be calculated by α_{ns}. In the experiment, the traditional balanced twin detector technique is applied to measure the saturated absorption of materials. Using a MLFL whose pulse duration is 200 fs and repetition rate is 110 MHz at 1550 nm as a seed source, the stable illuminant for measurement is obtained. The mode-locked pulses are divided into two channels of light with synchronous and adjustable intensity through a variable optical attenuator and a 3 dB coupler, which are used as test light and reference light respectively. The reference light can be directly measured by an optical power meter, while the test light is measured after passing through the sample. The blue dots in Fig. 1(g) is the data collected from 107 nm-SnS_2 SA. After theoretical fitting with formula (1) through red line, the exact values of various nonlinear parameters in formula (1) are determined. From Fig. 1(g), the I_{sat}, α_s and α_{ns} of 107 nm-SnS_2 SA are 0.68 MW/cm^2, 40.5% and 15%. Similarly, the I_{sat}, α_s and α_{ns} of 7.7 nm- and 4 nm-SnS_2 SAs are 1.3 MW/cm^2, 36.9%, 4.3% (Fig. 1(h)) and 0.52 MW/cm^2, 31.5%, 26% (Fig. 1(i)).

Results and discussion

Experimental setup

The components of the experimental device are shown in Fig. 2, including a 980 nm laser diode (LD), erbium-doped fiber (EDF), a SnS_2 SA, a 980/1550 wavelength division multiplexer (WDM), isolator (ISO), a polarization controller (PC) and a 80/20 optical coupler (OC).

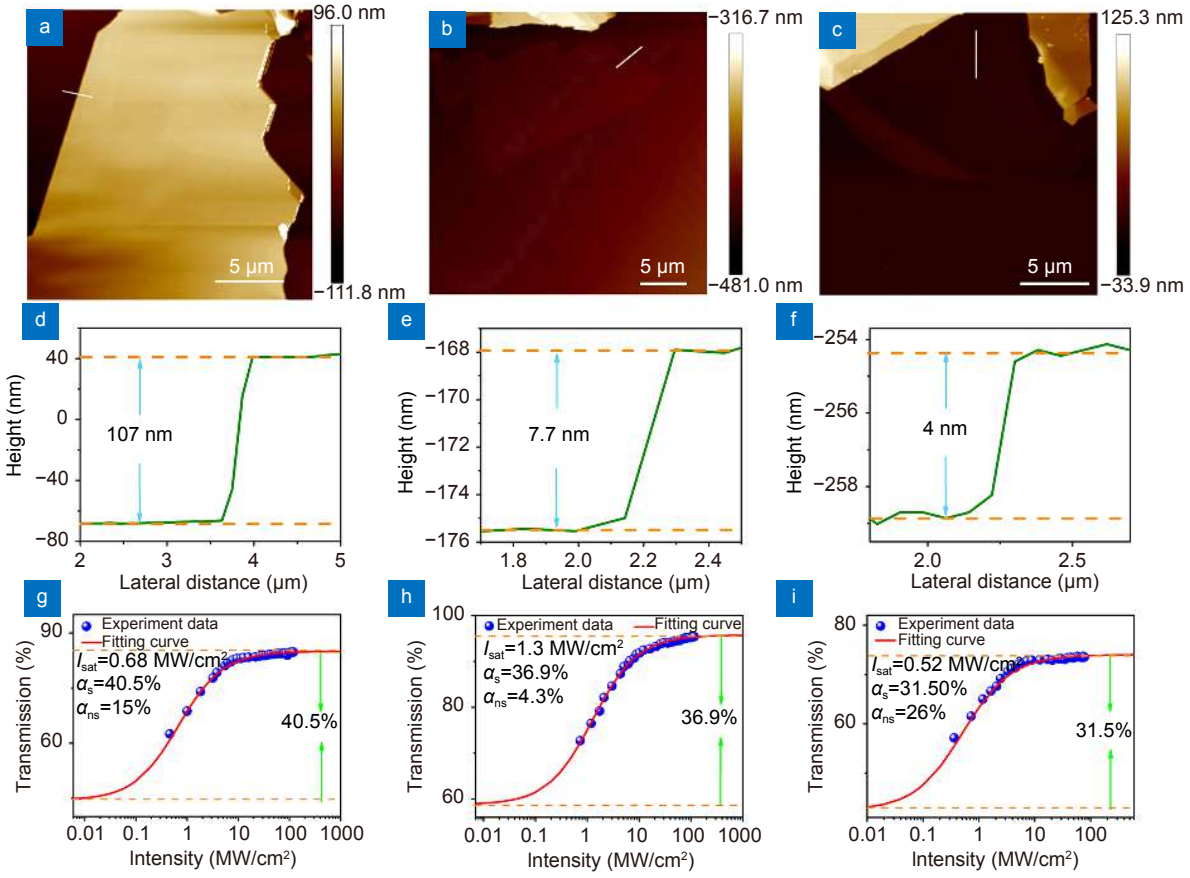

Fig. 1 | Characterization of materials. The AFM image, thickness and nonlinear absorption of (**a, d, g**)107 nm-SnS_2 SA, (**b, e, h**)7.7 nm-SnS_2 SA, (**c, f, i**)4 nm-SnS_2 SA.

LD provides pump light for the entire system, its maximum output power is 630 mW. WDM is used to synthesize a bunch of 980 nm pump light and 1550 nm light running in the cavity on a single fiber. After the excitation of pump light with high power density, 40 cm-EDF achieves the sufficient particle number reversal state, generating oscillating laser. The SnS_2 SA is the key optical modulation device in the cavity, fine tuning the PC to alter the polarization state of the laser and improve the laser quality. The ISO is used to ensure the consistency of the propagation direction of the ring laser. The OC delivers 20% of the intra-cavity laser to the outside of the cavity for real-time observation of the laser performance. The instruments used to measure the properties of QSFL are spectrometer (Yokogawa AQ6370C), spectrum analyzer (Agilent E4402B), and oscilloscope (Tektronix DPO3054).

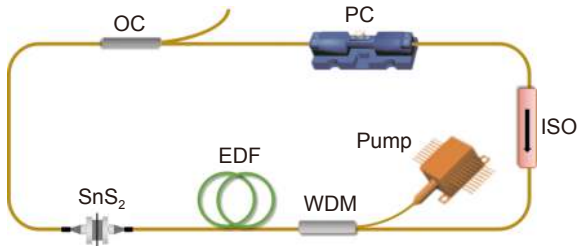

Fig. 2 | The simplified representation of QSFL based on SnS_2.

When 107 nm-SnS_2 SA is applied to the system, the performance of the QSFL is summarized in Fig. 3. At this time, the pump power (P_{pump}) of the laser is adjusted to the maximum, which is 630 mW. The pulse duration (τ) of a single pulse displayed on the oscilloscope is 484.7 ns as shown in Fig. 3(a). From the RF spectrum in Fig. 3(b), the fundamental frequency (F_{rep}) of pulse is ~240 kHz, the signal-to-noise ratio (SNR) is up to 50 dB. RF spectrum within a bandwidth of 2 MHz in illustration indicates that the QSFL works well. The spectrum of QSFL in Fig. 3(c) reveals that the wavelength is centered at 1530.6 nm. The standard deviation of output power (P_{out}) monitoring within 8 hours in Fig. 3(d) is 0.493 mW, which emphasized the constancy of the laser. When the P_{pump} is regulated, the traditional change trends of corresponding τ, F_{rep}, P_{out} and pulse energy (E_p) are respectively shown in Fig. 3(e) and 3(f). It is found that the threshold value of laser is 212 mW. The adjustment ranges of τ and F_{rep} are 0.485–1.4 μs and 141–241 kHz. The maximum of P_{out} is 12.7 mW, and the corresponding E_p is 52.6 nJ.

Next, the other two kinds of materials are also used to realize the Q-switched pulse under the same experimental conditions. For the Q-switched pulse under the same experimental conditions. For the QSFL using 7.7 nm-SnS_2 SA, the τ is 492.6 ns at the same pump power as shown in Fig. 4(a), which is slightly inferior to the laser based on 107 nm-SnS_2 SA. The standard deviation of P_{out} monitoring within 8 hours in Fig. 4(b) is 0.52 mW. From Fig. 4(c), the threshold value of laser is 276 mW, the τ and F_{rep} are adjustable in the range of 0.493–0.844 μs and 162 –240 kHz respectively. From Fig. 4(d), the maximum P_{out} and E_p are 14.3 mW and 59 nJ.

Similarly, the performances of QSFL employing 4 nm-SnS_2 SA are recorded in Fig. 5. The τ of the laser at the P_{pump} of 630 mW is 503.3 ns as shown in Fig. 5(a). The standard deviation of P_{out} within 8 hours is acknowledged in Fig. 5(b) as 0.543 mW. In Fig. 5(c), the adjustment range of τ and F_{rep} are revealed as 0.503 –1.25 μs and 123 –248 kHz. The boot threshold of laser is 180 mW. As show in Fig. 5(d), the maximum of P_{out} and E_p are obtained when the P_{pump} takes the maximum value of 630 mW, which are 11.3 mW and 45.7 nJ. In addition, each material has been repeatedly tested, eliminating the possibility of experimental error within our capabilities.

The performance of three different QSFLs adopting distinct SAs are summarized in Table 1. First of all, it is found that the nonlinear behavior of materials with different thickness is distinct. In terms of modulation depth, the 107 nm-SnS_2 owns the best performance. This may be related to the relaxation time. Generally, the material with larger relaxation time is beneficial to the enhancement of the modulation depth. Due to the large specific surface area and/or the presence of multiple edges shortening the lifetime of free carriers[32], the thin material tends to show a shorter relaxation time, so thicker materials show the maximum modulation depth in our experiments. The difference in the initial transmittance of the three materials may be the result of the

Table 1 | The performance of three different QSFLs adopting distinct SA.

SA	α_s/I_{sat}(MW/cm^2)	Threshold(mW)	τ(μs)	F_{rep} (kHz)	Stability (mW)	P_{out}(mW)	E_p(nJ)
107 nm-SnS_2	40.5%/0.68	212	0.485−1.4	141−241	0.493	12.7	52.6
7.7 nm-SnS_2	36.9%/1.3	276	0.493−0.844	162−240	0.52	14.3	59
4 nm-SnS_2	31.5%/0.52	180	0.503−1.25	123−248	0.543	11.3	45.7

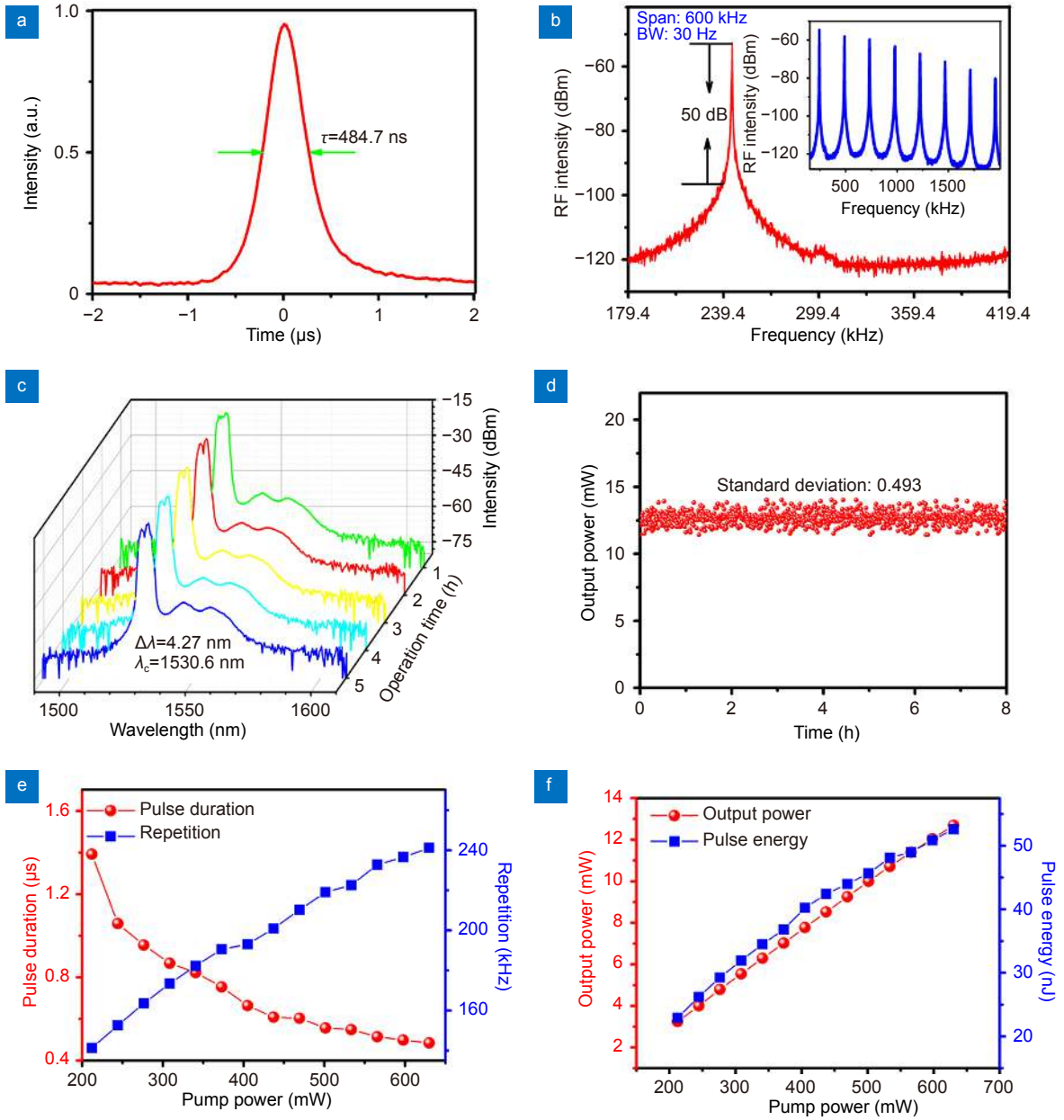

Fig. 3 | The function of the QSFL based on 107 nm-SnS_2 SA. (**a**) The τ of a single pulse. (**b**) RF spectrum (illustration: RF spectrum within a bandwidth of 2 MHz). (**c**) Emission spectrum. (**d**) The monitoring of P_{out} within 8 hours. (**e**) Variation of τ and F_{rep} as functions of P_{pump}. (**f**) Variation of P_{out} and E_p as functions of P_{pump}.

combined effect of scattering loss and carrier relaxation. With the change of thickness, the scattering loss and carrier relaxation have opposite effects on the transmittance, which leads to the existence of an optimal value to maximize the transmittance. The material with medium thickness (7.7 nm) exhibits the highest transmittance (~60%), which means that the material is closest to the equilibrium point among the three materials. The difference in the I_{sat} of three SAs may be due to the distinction in light utilization. Under the same initial light intensity, the light transmittance of 7.7 nm SnS_2 is the highest, which means that a lot of light goes directly through the material without being absorbed. If the material absorbs the same amount of light energy, the excitation intensity needs to be greater, so the 7.7 nm SnS_2 shows the largest saturation intensity.

The effect of SA with different nonlinearity on the performance of corresponding lasers is also obvious. The experimental results show that the output power based on SA with 40.5% modulation depth is the most stable (standard deviation: 0.493 mW), this is due to SA with high modulation depth can promote the stability of the

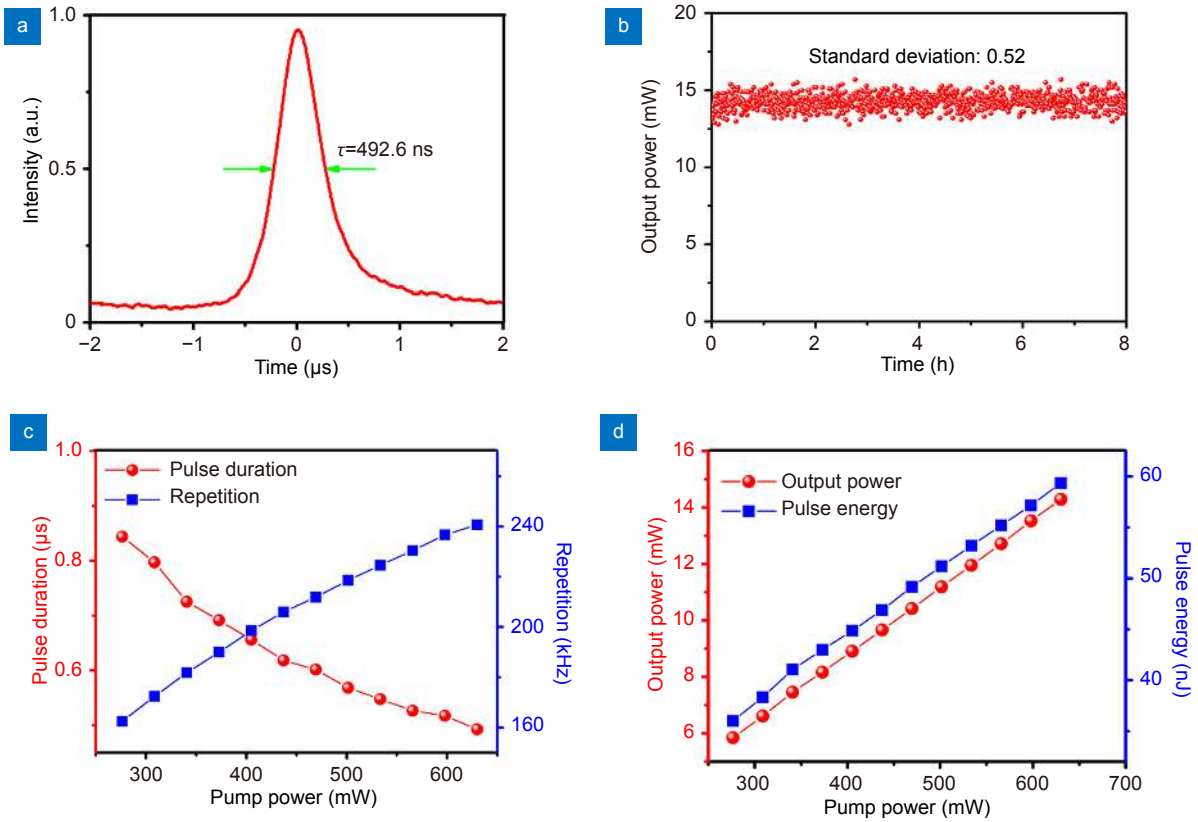

Fig. 4 | The performance of the QSFL based on 7.7 nm-SnS_2 SA. (**a**) The τ of a single pulse. (**b**) The monitoring of P_{out} within 8 hours. (**c**) Variation of τ and F_{rep} as functions of P_{pump}. (**d**) Variation of P_{out} and E_p as functions of P_{pump}.

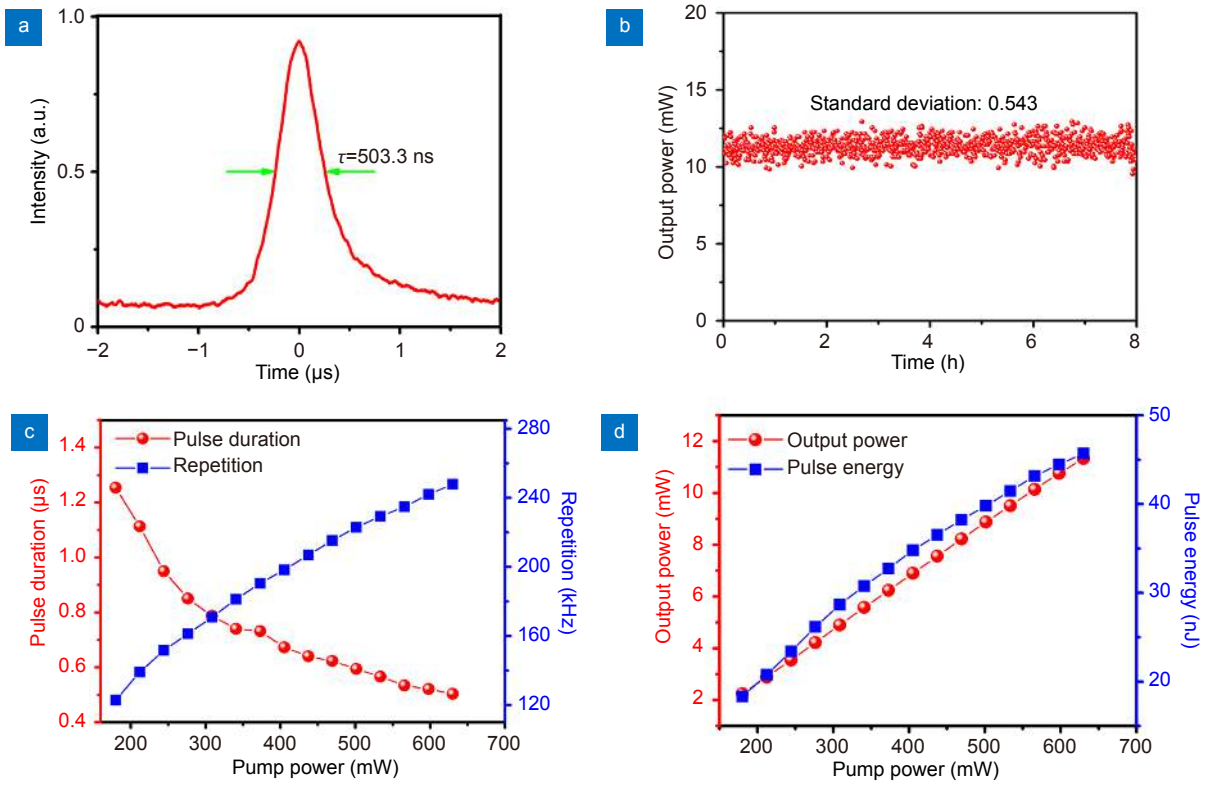

Fig. 5 | The performance of the QSFL based on 4 nm-SnS_2 SA. (**a**) The τ of a single pulse. (**b**) The monitoring of P_{out} within 8 hours. (**c**) Variation of τ and F_{rep} as functions of P_{pump}. (**d**) Variation of P_{out} and E_p as functions of P_{pump}.

system according to the previous research[33]. In addition, SA with large modulation depth seems to have a slight advantage in achieving short pulse. Because a large modulation depth means that the low-intensity signals at the leading and trailing edges of the pulse will be absorbed more, and the pulse narrowing effect will be stronger. Because SA with low saturation intensity is easy to saturate, the 4 nm-SnS_2 with saturation strength of 0.52 MW/cm^2 shows the the minimum threshold.

Currently, passive QSFLs based on various SAs have been extensively studied. Table 2 compares the performance of lasers based on several widely used SAs. By comparison, we find that SnS_2 SA seems to have some advantages in the realization of short pulse. Both the laser realized in ref[30], and the lasers obtained in this experiment show a pulse duration of about 500 ns, which is almost an order of magnitude better than other lasers. It is worth noting that the great disparity in modulation depth between SnS_2 in this experiment and PVA-SnS_2 in ref.[30] may be due to the difference in preparation methods. Crystal SnS_2 in our experiment is prepared using a combination of CVT and ME, therefore, it may perform better than PVA-SnS_2 in ref.[30] in terms of material quality, light reaction efficiency and scattering loss, which is beneficial to the enhancement of modulation depth. In addition, the output power of the laser obtained in this experiment is as high as 12.7 mW, and at the same time, the conversion rate of pump power to output power in the system is also more than 2%. This indicates that the laser based on SnS_2 can ensure high pump conversion efficiency under the condition of high power output. Therefore, in-depth investigation of SnS_2 has a bright prospect and practical value in the field of nonlinear optics.

Carrier mobility and electronic structure calculations of multi-layer SnS_2 with different thickness

Structure optimization and band structure calculations were performed based on density functional theory (DFT) as implemented in the Vienna ab-initio simulation package (VASP)[38–39]. The projector-augmented-wave (PAW) method was utilized to describe the interactions between the ionic cores and the valence electrons[40–41]. The Perdew-Burke-Ernzerhof parameterized generalized gradient approximation (PBE-GGA) functional was employed to treat the electronic exchange-correlation effects[42]. Electronic wave functions were expanded using a plane wave basis set with an energy cutoff of 340 eV. The thickness of vacuum layers was set to be at least 15 Å (1 Å=10^{-10} m) to avoid periodic interactions. The DFT-D3 method was adopted to include the van der Waals interactions during the structure relaxations[43]. The surface Brillouin zone was sampled using a Monkhorst-Pack grid[44]. The ionic relaxations were performed until the force on each atom was less than 0.005 eV·Å^{-1} and convergence criterion for the self-consistent electronic minimization loop was set to 10^{-5} eV. For accurate band gap prediction, the nonlocal Heyd-Scuseria-Ernzerhof hybrid functional (HSE06), which contains 25% Hartree-Fock and 75% PBE-GGA, is adopted for electronic structure calculations[45–46].

The relaxation time related to the carrier mobility μ, and μ in 2D semiconductor film of finite thickness is calculated based on the deformation potential[47–49]. The deformation limited mobility is calculated by[50]:

$$\mu_{\rm film} = \frac{\pi e\hbar^4 C_{\rm film}}{\sqrt{2}(k_{\rm B}T)^{3/2}(m^*)^{5/2}(D_A)^2}\cdot F\,, \tag{2}$$

where F is a crossover function that bridges 2D and 3D

$$F = \frac{\sum_n \left\{\frac{\sqrt{\pi}}{2}[1-{\rm erf}(\Omega(n))+\Omega(n){\rm e}^{-\Omega^2(n)}]\right\}}{\sum_n [1+\Omega^2(n)]{\rm e}^{-\Omega^2(n)}}\,. \tag{3}$$

Here, erf() represents the error function, and the summation over integer n is due to quantum confinement along the z-direction (finite thickness direction). $\Omega(n)$ is defined as

$$\Omega(n) = \sqrt{\frac{n^2\pi^2\hbar^2}{2m^* W_{\rm eff}^2 k_{\rm B}T}}\,, \tag{4}$$

Table 2 | Comparison of QSFL based on various SAs.

Materilas	α_s (%)	$\Delta\lambda/\lambda$(nm)	F_{rep}(kHz)	τ(μs)	P_{out}/P_{pump}(mW)	Threshold(mW)	E_p(nJ)	SNR(dB)	Refs.
Graphene	–	0.02/1539.6	10.36–41.8	3.89	<1.2/65	13.5	28.7	30	ref.[34]
BP	18.55	0.2/1562.87	6.983–15.78	13.2	~1.5/195	50	94.3	45	ref.[35]
WS_2	2.53	–/1560	47.03~77.93	3.96	6.41/650	400	1179.4	54.2	ref.[36]
MoS_2	2	–/1551.2	8.77–43.47	3.3	5.91/227	18.9	160	50	ref.[37]
SnS_2	3.15	0.03/1532.7	172.3–233.0	0.510	9.33/632	290	~40	50	ref.[30]
SnS_2	40.5	4.3/1530.6	141–241	0.485	12.7/630	180	45.7	50	This work

$W_{\rm eff}$ is the effective thickness of the film, which can be calculated analytically by assuming a square-well confinement potential.

In Eq. (2), $D_{\rm A}$ is the deformation potential, which is calculated from its definition $\delta E_i = D_{{\rm A}i}\frac{\delta_\alpha}{\alpha}$. δE_i is the energy change of the $i_{\rm th}$ electronic band under proper cell compression and dilatation, α is the lattice constant, and δ_α is the deformation of α. $C_{\rm film}$ is related to the elastic constant which is calculated from $\frac{\delta E_{\rm tot}}{V_0} = \frac{C_{\rm film}}{2}\left(\frac{\delta_\alpha}{\alpha}\right)^2$, where $\delta E_{\rm tot}$ refers to the total energy change and V_0 is the lattice volume at equilibrium. m^* is the effective mass along the transport direction. More computational details can be found in Kang's work[50]. The intrinsic carrier concentration in 2D semiconductor materials can be calculated by[51]:

$$n_i = \frac{\sqrt{m_h^* m_e^*}k_{\rm B}T}{\pi\hbar^2}\exp\left(-\frac{E_{\rm g}}{2k_{\rm B}T}\right), \qquad (5)$$

where $E_{\rm g}$ is the band gap. Our DFT calculations indicate that the electron mobility is thickness-dependent, it increases with increased thickness, and converges to bulk state when the thickness reaches either-layer as shown in Fig. 6.

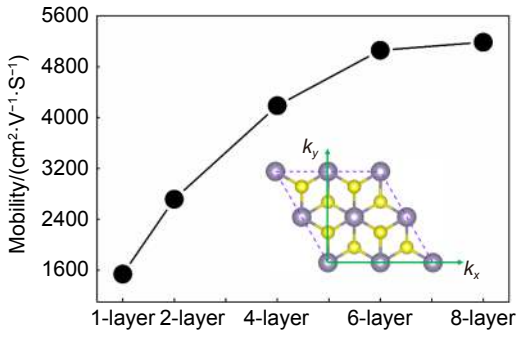

Fig. 6 | The DFT calculated deformation potential limited electron mobility along k_x direction of SnS_2 vs the number of SnS_2 layers.

The intrinsic carrier concentration is rather sensitive to the band gap and less sensitive to the variation of the effective mass. Due to the decreased band gap of SnS_2 with increased thickness, our DFT calculations in Table 3 clearly reveal that the intrinsic carrier concentration is significantly increased as the thickness increases, thus corresponding to the enhanced modulation depth.

Conclusions

In short, three kinds of SnS_2 with different thickness are characterized in terms of nonlinearity and used to realize the Q-switched pulses. The SnS_2 SA is prepared through the combination of CVT and ME to double guarantee the high quality of materials. By comparing the nonlinear performance of SnS_2 SA with different thickness, it is found that the thicker material shows higher modulation depth due to the influence of large relaxation time. Because of the combined effect of scattering loss and relaxation time, the initial transmission and thickness do not show a simple linear trend, but there is an optimal value. In addition, the saturation intensity is related to the initial transmittance of the material. Furthermore, the performances of the QSFLs with these three kinds of SA are compared. It is found that large modulation depth is beneficial to the stability of the laser, and at the same time, it seems to have a weak advantage in the realization of ultrashort pulse. A small saturation intensity of SA tends to make the laser have a small start threshold. In addition, combined with previous research, SnS_2 seems to have inherent advantages and potential in achieving ultrashort pulse. These results clarify the thickness-dependent nonlinear optical properties of SnS_2, and the impact of various optical nonlinear parameters of SA on the performance of the corresponding laser, which provides a meaningful reference for further research on the application of SnS_2 or similar TMDs materials in nonlinear optics.

Table 3 | The intrinsic carrier concentration (k_x) of SnS_2 vs the number of SnS_2 layers.

Thickness	Band gap	n_{ix} (m^{-2})
1-Layer	1.57 eV	$2.44\times10^{+3}$
2-Layer	1.52 eV	$6.74\times10^{+3}$
4-Layer	1.39 eV	$1.13\times10^{+5}$
6-Layer	1.34 eV	$4.73\times10^{+5}$
8-Layer	1.27 eV	$1.79\times10^{+6}$

References

1. Ma WZ, Zhao DS, Liu RM, Wang TS, Yuan Q et al. Observation and optimization of 2 μm mode-locked pulses in all-fiber net anomalous dispersion laser cavity. *Opto-Electron Adv* **3**, 200001 (2020).
2. Huang HZ, Li JH, Deng J, Ge Y, Liu HG et al. Passively Q-switched Tm/Ho composite laser. *Opto-Electron Adv* **3**, 190031 (2020).
3. Liu WJ, Liu ML, Ouyang YY, Hou HR, Lei M et al. CVD-grown $MoSe_2$ with high modulation depth for ultrafast mode-locked erbium-doped fiber laser. *Nanotechnology* **29**, 394002 (2018).
4. Zhang XJ, Li WW, Li J, Xu HY, Cai ZP, Luo ZQ. Mid-infrared all-fiber gain-switched pulsed laser at 3 μm. *Opto-Electron Adv* **3**, 190032 (2020).
5. Liu WJ, Liu ML, Liu B, Quhe RG, Lei M et al. Nonlinear optical properties of MoS_2-WS_2 heterostructure in fiber lasers. *Opt*

Express **27**, 6689–6699 (2019).
6. Wu K, Zhang XY, Wang J, Li X, Chen JP. WS_2 as a saturable absorber for ultrafast photonic applications of mode-locked and Q-switched lasers. *Opt Express* **23**, 11453–11461 (2015).
7. Liu ML, Ouyang YY, Hou HR, Liu WJ. Q-switched fiber laser operating at 1.5 μm based on WTe_2. *Chin Opt Lett* **17**, 020006 (2019).
8. Liu WJ, Liu ML, Han HN, Fang SB, Teng H et al. Nonlinear optical properties of WSe_2 and $MoSe_2$ films and their applications in passively *Q*-switched erbium doped fiber lasers. *Photonics Res* **6**, C15–C21 (2018).
9. Sun Q, Yu H, Ueno K, Zu S, Matsuo Y et al. Revealing the plasmon coupling in gold nanochains directly from the near field. *Opto-Electron Adv* **2**, 180030 (2019).
10. Hakulinen T, Okhotnikov OG. 8 ns fiber laser *Q* switched by the resonant saturable absorber mirror. *Opt Lett* **32**, 2677–2679 (2007).
11. Zhang H, Tang DY, Zhao LM, Bao QL, Loh KP. Large energy mode locking of an erbium-doped fiber laser with atomic layer graphene. *Opt Express* **17**, 17630–17635 (2009).
12. Bao QL, Zhang H, Wang Y, Ni ZH, Yan YL et al. Atomic-layer graphene as a saturable absorber for ultrafast pulsed lasers. *Adv Funct Mater* **19**, 3077–3083 (2009).
13. Sun ZP, Martinez A, Wang F. Optical modulators with 2D layered materials. *Nat. Photonics* **10**, 227–238 (2016).
14. Liu ML, Liu WJ, Wei ZY. $MoTe_2$ saturable absorber with high modulation depth for erbium-doped fiber laser. *J Lightwave Technol* **37**, 3100–3105 (2019).
15. Guo B, Wang SH, Wu ZX, Wang ZX, Wang DH et al. Sub-200 fs soliton mode-locked fiber laser based on bismuthene saturable absorber. *Opt Express* **26**, 22750–22760 (2018).
16. Lu SB, Miao LL, Guo ZN, Qi X, Zhao CJ et al. Broadband nonlinear optical response in multi-layer black phosphorus: an emerging infrared and mid-infrared optical material. *Opt Express* **23**, 11183–11194 (2015).
17. Liu WJ, Liu ML, Lin S, Liu JC, Lei M et al. Synthesis of high quality silver nanowires and their applications in ultrafast photonics. *Opt Express* **27**, 16440–16448 (2019).
18. Yan PG, Chen H, Yin JD, Xu ZH, Li JR et al. Large-area tungsten disulfide for ultrafast photonics. *Nanoscale* **9**, 1871–1877 (2017).
19. Liu ML, Ouyang YY, Hou HR, Lei M, Liu WJ et al. MoS_2 saturable absorber prepared by chemical vapor deposition method for nonlinear control in Q-switching fiber laser. *Chin Phys B* **27**, 084211 (2018).
20. Seo JW, Jang JT, Park SW, Kim C, Park B et al. Two-dimensional SnS_2 nanoplates with extraordinary high discharge capacity for lithium ion batteries. *Adv Mater* **20**, 4269–4273 (2008).
21. Feng TC, Zhang D, Li XH, Abdul Q, Shi ZJ et al. SnS_2 nanosheets for Er-doped fiber lasers. *ACS Appl Nano Mater* **3**, 674–681 (2020).
22. Niu KD, Sun RY, Chen QY, Man BY, Zhang HN. Passively mode-locked Er-doped fiber laser based on SnS_2 nanosheets as a saturable absorber. *Photonics Res* **6**, 72–76 (2018).
23. Huang Y, Sutter E, Sadowski JT, Cotlet M, Monti OLA et al. Tin disulfide-an emerging layered metal dichalcogenide semiconductor: materials properties and device characteristics. *ACS Nano* **8**, 10743–10755 (2014).
24. Song HS, Li SL, Gao L, Xu Y, Ueno K et al. High-performance top-gated monolayer SnS_2 field-effect transistors and their integrated logic circuits. *Nanoscale* **5**, 9666–9670 (2013).
25. Zhong HX, Yang GZ, Song HW, Liao QY, Cui H et al. Vertically aligned graphene-like SnS_2 ultrathin nanosheet arrays: excellent energy storage, catalysis, photoconduction, and field-emitting performances. *J Phys Chem C* **116**, 9319–9326 (2012).
26. Li S, Yin Y, Ouyang QY, Chen YJ, Lewis E et al. Dissipative soliton generation in Er-doped fibre laser using SnS_2 as a saturable absorber. *Appl Phys Express* **12**, 102008 (2019).
27. Li S, Yin Y, Ran GC, Ouyang QY, Chen YJ et al. Dual-wavelength mode-locked erbium-doped fiber laser based on tin disulfide thin film as saturable absorber. *J Appl Phys* **125**, 243104 (2019).
28. Gao JJ, Zhou Y, Liu YJ, Han XL, Guo QX et al. Noise-like mode-locked Yb-doped fiber laser in a linear cavity based on SnS_2 nanosheets as a saturable absorber. *Appl Optics* **58**, 6007–6011 (2019).
29. Liu WJ, Liu ML, Wang XT, Shen T, Chang GQ et al. Thickness-dependent ultrafast photonics of SnS_2 nanolayers for optimizing fiber lasers. *ACS Appl Nano Mater* **2**, 2697–2705 (2019).
30. Niu KD, Chen QY, Sun RY, Man BY, Zhang HN. Passively Q-switched erbium-doped fiber laser based on SnS_2 saturable absorber. *Opt Mater Express* **7**, 3934–3943 (2017).
31. Seo W, Shin S, Ham G, Lee J, Lee S et al. Thickness-dependent structure and properties of SnS_2 thin films prepared by atomic layer deposition. *Jpn J Appl Phys* **56**, 031201 (2017).
32. Kushnir K, Morissette E, Giri B, Doiron CW, Grimm RL et al. Carrier dynamics in SnS_2 single crystals and vertical nanostructures: role of edges. In *Proceedings of the 43rd International Conference on Infrared*, *Millimeter*, *and Terahertz Waves* (IRMMW-THz, 2018) (IEEE, 2018);http://doi.org/10.1109/IRMMW-THz.2018.8509909.
33. Hönninger C, Paschotta R, Morier-Genoud F, Moser M, Keller U. Q-switching stability limits of continuous-wave passive mode locking. *J Opt Soc Am B* **16**, 46–56 (1999).
34. Wang JZ, Luo ZQ, Zhou M, Ye CC, Fu HY et al. Evanescent-light deposition of graphene onto tapered fibers for passive Q-switch and mode-locker. *IEEE Photonics J* **4**, 1295–1305 (2012).
35. Chen Y, Jiang GB, Chen SQ, Guo ZN, Yu XF et al. Mechanically exfoliated black phosphorus as a new saturable absorber for both Q-switching and Mode-locking laser operation. *Opt Express* **23**, 12823–12833 (2015).
36. Chen BH, Zhang XY, Wu K, Wang H, Wang J et al. Q-switched fiber laser based on transition metal dichalcogenides MoS_2, $MoSe_2$, WS_2, and WSe_2. *Opt Express* **23**, 26723–26737 (2015).
37. Huang YZ, Luo ZQ, Li YY, Zhong M, Xu B et al. Widely-tunable, passively Q-switched erbium-doped fiber laser with few-layer MoS_2 saturable absorber. *Opt Express* **22**, 25258–25266 (2014).
38. Kresse G, Furthmüller J. Efficiency of ab-initio total energy calculations for metals and semiconductors using a plane-wave basis set. *Comput Mater Sci* **6**, 15–50 (1996).
39. Kresse G, Furthmüller J. Efficient iterative schemes for *ab initio* total-energy calculations using a plane-wave basis set. *Phys Rev B* **54**, 11169–11186 (1996).
40. Blöchl PE. Projector augmented-wave method. *Phys Rev B* **50**,

17953–17979 (1994).
41. Kresse G, Joubert D. From ultrasoft pseudopotentials to the projector augmented-wave method. *Phys Rev B* **59**, 1758–1775 (1999).
42. Perdew JP, Burke K, Ernzerhof M. Generalized gradient approximation made simple. *Phys Rev Lett* **77**, 3865–3868 (1996).
43. Grimme S, Antony J, Ehrlich S, Krieg H. A consistent and accurate *ab initio* parametrization of density functional dispersion correction (DFT-D) for the 94 elements H-Pu. *J Chem Phys* **132**, 154104 (2010).
44. Monkhorst HJ, Pack JD. Special points for Brillouin-zone integrations. *Phys Rev B* **13**, 5188–5192 (1976).
45. Heyd J, Scuseria GE, Ernzerhof M. Hybrid functionals based on a screened Coulomb potential. *J Chem Phys* **118**, 8207–8215 (2003).
46. Heyd J, Scuseria GE, Ernzerhof M. Erratum. Hybrid functionals based on a screened Coulomb potential [J. Chem. Phys. 118, 8207 (2003)]. *J Chem Phys* **124**, 219906 (2006).
47. Bardeen J, Shockley W. Deformation potentials and mobilities in non-polar crystals. *Phys Rev* **80**, 72–80 (1950).
48. Bruzzone S, Fiori G. *Ab-initio* simulations of deformation potentials and electron mobility in chemically modified graphene and two-dimensional hexagonal boron-nitride. *Appl Phys Lett* **99**, 222108 (2011).
49. Qiao JS, Kong XH, Hu ZX, Yang F, Ji W. High-mobility transport anisotropy and linear dichroism in few-layer black phosphorus. *Nat Commun* **5**, 4475 (2014).
50. Kang P, Michaud-Rioux V, Kong XH, Yu GH, Guo H. Calculated carrier mobility of h-BN/γ-InSe/h-BN van der Waals heterostructures. *2D Mater* **4**, 045014 (2017).
51. Shao ZG, Ye XS, Yang L, Wang CL. First-principles calculation of intrinsic carrier mobility of silicene. *J Appl Phys* **114**, 093712 (2013).

Acknowledgements

We acknowledge the financial support from the National Natural Science Foundation of China (11875008, 12075034); Open Research Fund of State Key Laboratory of Pulsed Power Laser Technology (Grant SKL2019KF04); Fundamental Research Funds for the Central Universities (2019XD-A09-3).

Author contributions

All authors commented on the manuscript. M. L. Liu, X. M. Liu, and Y. R. Wang performed the measurements and designed the project.W. J. Liu, M. Lei, and Z. Y. Wei fabricated the samples and performed the AFM results. H. B. Wu and W. Guo developed the theory. All authors discussed the result and contributed to the writing of the manuscript.

Competing interests

The authors declare no competing financial interests.